

Article

Improved Algorithms for Remote Sensing-Based Aerosol Retrieval during Extreme Biomass Burning Events

Sonoyo Mukai ^{1,*}, Itaru Sano ² and Makiko Nakata ³

- ¹ School of Applied Information Technology, The Kyoto College of Graduate Studies for Informatics, Sakyo, Kyoto 606-8225, Japan
- ² Faculty of Science and Technology, Kindai University, Higashi-Osaka 577-8502, Japan; sano@info.kindai.ac.jp
- ³ Faculty of Applied Sociology, Kindai University, Higashi-Osaka 577-8502, Japan; nakata@socio.kindai.ac.jp
- * Correspondence: s_mukai@kcg.ac.jp

Abstract: This study proposed an aerosol characterization process using satellites for severe biomass burning events. In general, these severely hazy cases are labeled as “undecided” or “hazy.” Because atmospheric aerosols are significantly affected by factors such as air quality, global climate change, local environmental risk, and human and biological health, efficient and accurate algorithms for aerosol retrieval are required for global satellite data processing. Our previous classification of aerosol types was based primarily on near-ultraviolet (UV) data, which facilitated subsequent aerosol retrieval. In this study, algorithms for aerosol classification were expanded to events with serious biomass burning aerosols (SBBAs). Once a biomass burning event is identified, the appropriate radiation simulation method can be applied to characterize the SBBAs. The second-generation global imager (SGLI) on board the Japanese mission JAXA/Global Change Observation Mission-Climate contains 19 channels, including red (674 nm) and near-infrared (869 nm) polarization channels with a high resolution of 1 km. Using the large-scale wildfires in Kalimantan, Indonesia in 2019 as an example, the complementarity between the polarization information and the nonpolarized radiance measurements from the SGLI was demonstrated to be effective in radiation simulations for biomass burning aerosol retrieval. The retrieved results were verified using NASA/AERONET ground-based measurements, and then compared against JAXA/SGLI/L2-version-1 products, and JMA/Himawari-8/AHI observations.

Keywords: GCOM-C/SGLI; satellite; severe biomass burning aerosols; radiative transfer



Citation: Mukai, S.; Sano, I.; Nakata, M. Improved Algorithms for Remote Sensing-Based Aerosol Retrieval during Extreme Biomass Burning Events. *Atmosphere* **2021**, *12*, 403. <https://doi.org/10.3390/atmos12030403>

Academic Editor: Ying Tsai

Received: 20 February 2021

Accepted: 16 March 2021

Published: 20 March 2021

Publisher's Note: MDPI stays neutral with regard to jurisdictional claims in published maps and institutional affiliations.



Copyright: © 2021 by the authors. Licensee MDPI, Basel, Switzerland. This article is an open access article distributed under the terms and conditions of the Creative Commons Attribution (CC BY) license (<https://creativecommons.org/licenses/by/4.0/>).

1. Introduction

Since 2019, large-scale forest fires have occurred in many parts of the world, including the Amazon, Australia, the west coast of North America, Siberia, and Indonesia. Consequently, large amounts of biomass burning aerosols (BBAs) have been released into the atmosphere [1–5], causing air pollution and adversely affecting the health and social lives of humans. The occurrence of forest fires has increased because of global warming and climate change. It has been reported that aerosols both directly and indirectly affect the climate [6–8] by contributing negatively and positively to surface temperature and cloud cover, respectively. Thus, the Fifth Intergovernmental Panel on Climate Change (IPCC) report on global warming (<https://www.ipcc.ch/report/ar5/wg1/> accessed on 14 February 2021) emphasized the importance of investigating aerosol characteristics and the dependency of positive or negative radiative effects on aerosol types [9,10]. The Fifth IPCC report also highlighted the warming effect of black carbon aerosols as opposed to the cooling effect of other aerosol types. Accurately detecting aerosol types has become critical for understanding global climate problems. Furthermore, large-scale wildfires and global warming are interdependent [11,12]. Thus, carbonaceous aerosols, such as smoke, soot, and black/brown carbon, should be rigorously defined. Note that, herein, carbonaceous aerosols generated by wildfires are collectively referred to as BBAs. Not

limited to carbonaceous particles, aerosol properties vary spatially and seasonally as a result of various factors, such as emissions, photochemical reactions, and wind direction. Characteristics and distribution of atmospheric aerosols are complex [13] and, to date, have not yet been sufficiently elucidated.

In this study, we used remote sensing to evaluate intense loadings of BBAs, which are unusual phenomena and known as severe aerosol events. Aerosol events deteriorate air quality, the environment, and human life, and are composed of not only biomass burning plumes but also other aerosol-type events. Atmospheric particles originate from natural or human activities. Mineral dust aerosols (dust) are the most dominant among the naturally originating aerosols. They are primarily emitted from the desert and are the most dynamic natural phenomena, often known as dust storms. During dust storms, large amounts of mineral dust particles are emitted into the atmosphere and subsequently widely transported, causing serious atmospheric turbidity [14,15]. Because the Sahara is the most well-known originator of dust emissions, dust aerosols are known as Saharan dust [16,17]. In Asia, yellow sand causes widespread, severe air pollution [18,19]. Further, it is highly likely that large-scale aerosol events due to a combination of both natural factors and human activities have occurred [20]. While these phenomena should be considered in future studies, this study specifically addresses severe biomass burning plumes.

The Japanese mission JAXA/GCOM (Global Change Observation Mission-Climate)-C (SHIKISAI in Japanese) launched in 2017 carried a second-generation global imager (SGLI). The SGLI is a multispectral sensor that includes near-ultraviolet (UV) and two polarization channels. It contains 19 channels from near-UV to thermal infrared (IR), including red (674 nm named PL1 band) and near-IR (869 nm; PL2 band) polarization channels. This study demonstrates the advantages of the SGLI in detecting and characterizing BBAs during severe wildfire events. Previous studies [21,22] have shown that near-UV data at 412 and 380 nm wavelength channels not only revealed absorbing aerosols, such as BBAs or dust, but were also used to distinguish BBAs and dust using short-wavelength IR measurements at 1063 nm [22]. Further, a 2210 nm channel was employed using observations from the Advanced Earth Observing Satellite (ADEOS)-2/Global imager (GLI) [21]. As understanding aerosol types facilitates subsequent aerosol retrieval, algorithms for aerosol classification were expanded to severe BBAs (SBBAs) herein. Severe hazy cases are often left unprocessed and labeled as “undecided” or “hazy.” Hence, aerosols must be characterized without omission, particularly for satellite data on a global scale. Therefore, in this study, the compatibility between polarization and nonpolarization information was investigated, and both were used effectively for SBBA characterization.

A brief review of the previously proposed classification algorithm for land aerosol types and the detection of new types of SBBAs is detailed in Section 2. After identification, SBBAs were characterized using radiation simulations. The aerosol retrieval method is described in Section 3. The outline of aerosol retrieval, aerosol modeling, and the radiative transfer (RT) method are also explained. Section 4 considers severe wildfires in Asia that cause severe air pollution and adversely affect both humans and the environment. In particular, an example of the Kalimantan wildfire in Indonesia on 15 September 2019 is examined. First, an RT method named successive order of scattering for a semi-infinite atmosphere model [23] is applied for radiation simulation around the area of the severe wildfire event. Subsequently, a vector type adding–doubling method is adopted [24]. The results show that the SGLI radiance and polarization measurements can effectively characterize the aerosols in the central area that contributed to the severe biomass burning in the vicinity of the target area. Sections 5 and 6 discuss the results and provide the study conclusions, respectively.

2. Detecting SBBAs

In a previous study, aerosol type classification was performed using an SGLI mounted on the Japanese mission JAXA/Global Change Observation Mission-Climate (GCOM-C; SHIKISAI in Japanese) [25]. Aerosols over land can be classified into three types:

carbonaceous aerosols, dust particles, and sulfate aerosols [26,27]. However, complicated mixtures of each type exist in nature. In this study, BBAs and dust were presented as typical examples of carbonaceous aerosols and dust particles, respectively. Absorbing aerosols, such as BBAs and dust, can be effectively detected using UV wavelengths, which has been demonstrated using data from the Total Ozone Mapping Spectrometer (TOMS) on the Nimbus-7 satellite in 1978 [28]. Our previous works [21,22] were based on a similar concept to TOMS-AI (aerosol index). Thus, in accordance with these studies, we referred to this concept as the absorbing aerosol index (AAI) [21].

$$AAI = R(412)/R(380). \quad (1)$$

The variable R in Equation (1) represents the satellite-observed reflectance value at the near-UV (380 nm) and violet (412 nm) wavelength channels. This variable was added to avoid ambiguity as the definition of AAI differs from that employed by the TOMS or Global Ozone Monitoring Experiment [29] in the equation and reference channels, in which they employ a shorter wavelength (340 nm) than that used in Equation (1). In addition, AAI has a simpler form as it is simply the ratio of the reflectance. The derivation of Equation (1) is provided in our previous work [21]. Briefly, the AAI for aerosol type identification assumes a fairly optically thick atmosphere, such as an aerosol optical thickness (AOT (550 nm) ≥ 1), because the satellite observes scattered radiation via atmospheric particles, reflected radiation from the Earth's surface, and their interaction. However, the contribution of surface reflection to the satellite data decreases with increasing AOT, and thus an AOT (550 nm) of 1 was selected as a suitable value for the threshold of negligible bottom reflection. As the contribution of Rayleigh scattering becomes smaller in such an optically thick atmosphere, we decided to use the simple form of Equation (1) for the AAI.

However, the AAI cannot distinguish BBAs from dust as shortwave IR wavelengths only detect dust aerosols [22,30]. Subsequently, in a manner similar to Equation (1), the ratio of reflectance at wavelengths of 1630 nm to 380 nm was defined as the dust detection index (DDI).

$$DDI = R(1630)/R(380). \quad (2)$$

The Japanese satellite GCOM-C was launched on 23 December 2017 and mounted with only the SGLI multispectral sensor, containing 19 channels encompassing near-UV (380 nm) and violet (412 nm) wavelengths, and two polarization channels PL1 and PL2 in red (674 nm) and near-IR (869 nm) wavelengths. The instantaneous field-of-view (IFOV) of the SGLI is extremely fine: 250 m in the near-UV to short-IR wavelength range, and 1 km for the polarization measurements. Note that this polarization measurement is the smallest resolution obtained to date. The SGLI measurements can be performed using Equations (1) and (2).

Figure 1 shows a discrimination chart of aerosol types as "BBA," "dust," and "others" obtained from the GCOM-C/SGLI/L2 data, for BBAs selected over BBA-domain areas, such as the Amazon, South Africa, and Siberia, from May to October in 2018 and May to August in 2019, and for dusts selected over the Sahara Desert from May 2018 to August 2019. The total amount of data was sufficient for statistical processing, reaching $\geq 1,000,000$ BBA sampling data, and $\geq 3,000,000$ dust data [22]. These data did not include cloud pixels because they were excluded from the SGLI/L2-cloud flag products. As shown in Figure 1, sulfate-based aerosols and all the mixed cases were classified as "others". The "others" type is the most common aerosol type in nature. The idea is that the aerosol retrieval process is to determine the aerosol properties of each satellite pixel by pixel, but if we can approximate the typical BBA and dust as a preprocessing step, the aerosol retrieval process will be more efficient. In this study, aerosol type discrimination was not addressed. However, a new aerosol type named "SBBA" was proposed, which represents BBAs during extremely intense biomass combustion. To derive the threshold values of the AAI and DDI in order to discriminate the SBBA category, the SGLI data for the period from September 2019 to June 2020 were included in this study.

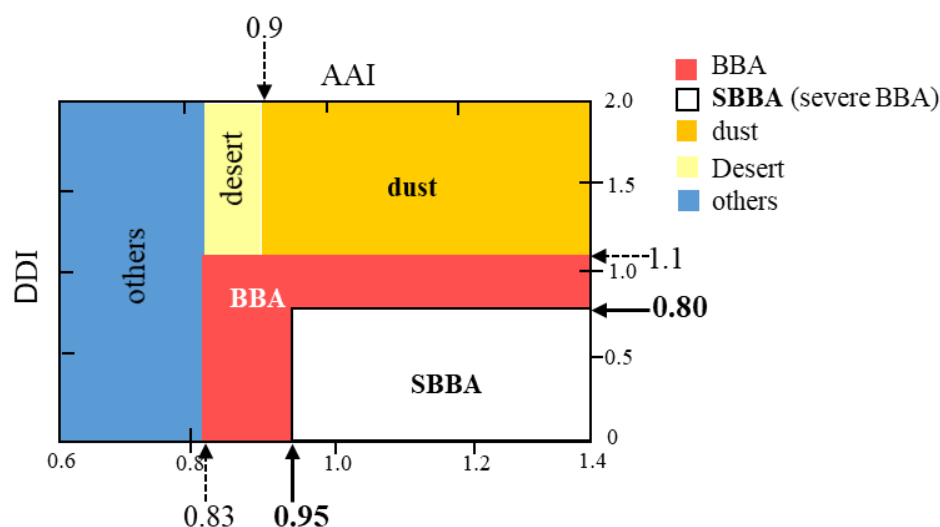


Figure 1. Continental aerosol type classification chart. Horizontal and vertical axes denote AAI and DDI values, respectively. Aerosol type category is shown in the upper right key. Some data was obtained from a previous study [22].

Figure 2 shows practical examples of extremely severe biomass burning events observed by the SGLI. The examples of sampling areas are denoted as A, B, C, and D, as shown on the world map at the top. The details of each area are as follows: A: Western Canada on 14 August 2018; B: Siberia on 7 August 2019; C: Indonesia on 25 September 2019; and D: Brazil on 14 September 2020. Each sample comprises a set of five figures. Figure 2a–c shows the color composite image, AAI distribution, and histogram, respectively, within the region of interest indicated by the white rectangle in the distribution map, followed by the DDI and AAI from left to right. The color composite image clearly indicates that a fire disaster occurred, causing heavy smoke, wherein SBBAs are depicted as a smoky gray. As shown in Figure 2, the histograms show that the heavy smoke regions coincide with regions with AAI values exceeding 0.95, and DDI values less than 0.80. Therefore, the proposed SBBA discrimination diagram shown in Figure 1 was validated for several heavy smoke scenes based on the GCOM-C/SGLI measurements.

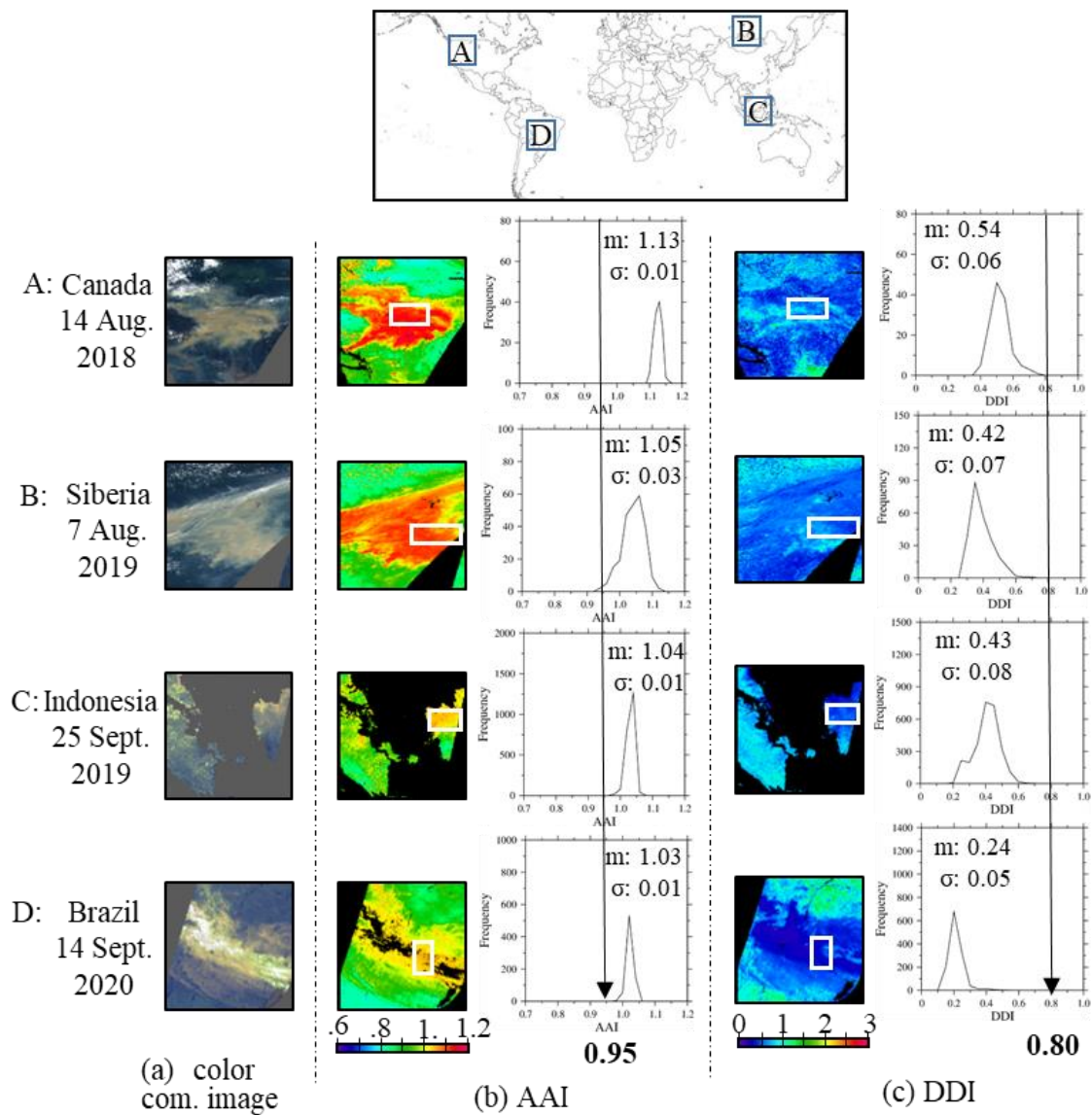


Figure 2. Examples of extremely severe biomass burning observed by the global change observation mission-climate/second-generation global imager (GCOM-C/SGLI). Each sample comprises a set of five figures. (a) Color composite image, (b) absorbing aerosol index (AAI), and (c) dust detection index (DDI) distributions, wherein the histogram within the region is indicated with a white rectangle in the distribution map.

3. Method of Aerosol Retrieval

3.1. Method Framework

Figure 3 shows the block flow of aerosol retrieval from space employed in this study. First, the constituents of the combined system of Earth’s atmosphere surface must be modeled. Atmospheric molecules and the earth’s surface are described according to the low-resolution atmospheric transmission-7 and International Geosphere-Biosphere Program, respectively. Aerosol modeling is a fundamental element of this process as predicting the aerosol type helps to create an appropriate aerosol model. Therefore, to enable efficient aerosol retrieval, we classified the aerosol types proposed in Section 2, and the aerosol modeling emphasized in section [A] in the bottom left table of Figure 3 is described in detail in Section 3.2.

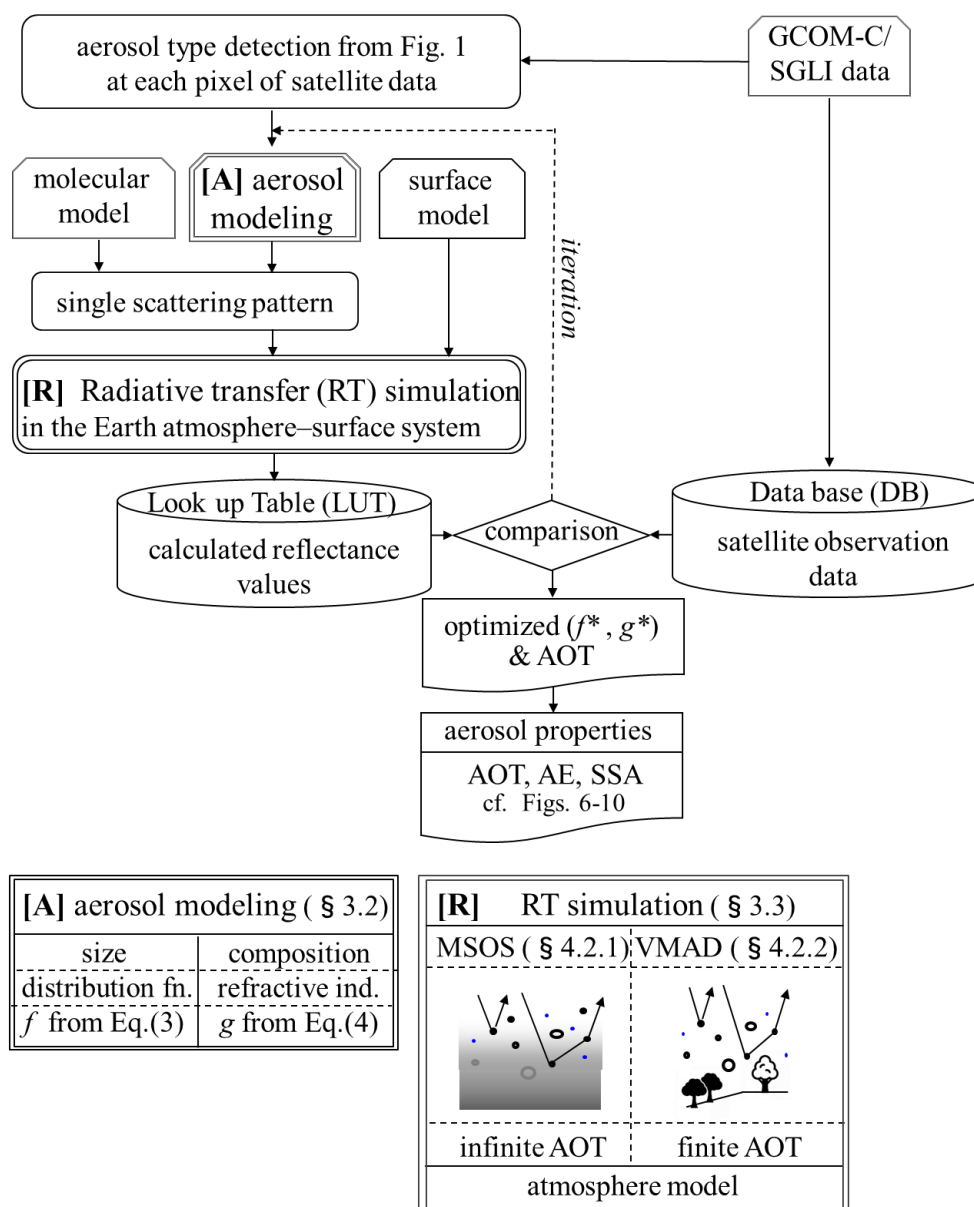


Figure 3. Basic framework and block flow of our aerosol retrieval method. The aerosol properties AOT, AE and SSA denote aerosol optical thickness, Ångström exponent and single scattering albedo, respectively. MSOS and VMAD of RT method represent method of successive order of scattering and vector method of adding-doubling, respectively.

The next step is the radiation simulation of the Earth’s atmosphere–surface system. Once the upwelling radiance at the top of the atmosphere corresponding to the measurements of the space-borne sensor—which is the reflectance from the combined system of the Earth’s atmosphere surface—is calculated, it is stored in a look-up table (LUT). Meanwhile, the satellite data are stored in a database (DB) after they are converted to a format suitable for use. The LUT and DB values are compared iteratively at each pixel of the satellite data to derive the final optimized aerosol parameters. The RT simulations, denoted by [R] in Figure 3, are detailed in Section 3.3.

3.2. Aerosol Modeling

Atmospheric aerosols vary widely in space and time in terms of both quantity and quality. Therefore, in this study, we focused on extremely dense BBAs and their characteristics. The terms related to aerosol properties are briefly explained as follows. The most basic characteristic of aerosols is their spectral aerosol optical thickness $AOT(\lambda)$ at

wavelength λ [20]. The Ångström exponent (AE) is derived from the spectral AOT(λ) and is closely related to the aerosol size [26]. First, the aerosol sizes are investigated, and the size distributions are assumed to be two modes (fine and coarse) in a bimodal log-normal distribution of the particle volume (V) with six parameters (volume concentration, mode radius, and the standard deviation of the fine and coarse mode particles) [27]. Too many parameters are excessive for the retrieval of the optimized aerosol sizes especially at a global scale. Then, the aerosol size distribution function is simplified [23], enabling the size distribution function for continental aerosols to be approximately defined by the unique variable of the fine particle fraction (f) of the volume concentration, as follows:

$$\frac{dV}{d \ln r} = \frac{f}{\sqrt{2\pi} \ln 1.533} \exp\left[-\frac{(\ln r - \ln 0.144)^2}{2 \ln^2 1.533}\right] + \frac{(1-f)}{\sqrt{2\pi} \ln 2.104} \exp\left[-\frac{(\ln r - \ln 3.607)^2}{2 \ln^2 2.104}\right]. \tag{3}$$

The next aerosol characteristic of interest is the refractive index. Mixing of many kinds of particles is one of the major challenges in the analysis of aerosol characteristics. Although, in reality, mixing of particles is not limited to external or internal mixing, but more practical mixing should be considered, taking into account meteorological conditions and particle composition and shape, a simple homogeneous internal two-component mixing model was adopted here, wherein the Maxwell Garnett mixing (MGM) rule was used [31]. The MGM rule provides a complex refractive index as follows:

$$\varepsilon = \varepsilon_m \frac{(\varepsilon_j + 2\varepsilon_m) + 2g(\varepsilon_j - \varepsilon_m)}{(\varepsilon_j + 2\varepsilon_m) - g(\varepsilon_j - \varepsilon_m)}, \tag{4}$$

where ε denotes the dielectric constant, subscripts m and j represent the matrix and inclusion, respectively, and g represents the volume fraction of the inclusions. The values of $1.410-0.004i$ and $1.520-0.035i$ were used for the matrix and inclusions, respectively, in the BBA characterization calculations using the SGLI data. We have confirmed that it is possible to interpret the case of growing process from aerosol to fog by reducing the ratio of inclusion (g) and shifting the size toward the coarse mode (namely reducing f value). This implies that SBBAs can be described using two parameters (f and g). The details of which have been described in a previous study [21]. Note that g depends on the wavelength (λ). Thus, spectral absorption (i.e., the imaginary part of the refractive index) must be considered, especially for near-UV wavelengths [32,33]. However, the wavelength dependence of the refractive index is not very strong for BBAs in the visible band. Therefore, the value of g is assumed to be constant in the visible wavelength region, wherein $g1$ is used for near-UV, $g2$ for visible, and $g3$ is used for near-IR channels in this work.

3.3. RT Simulation Method

Multiple light scattering in the Earth’s atmosphere–surface system must be simulated to determine the characteristics of aerosols. Numerical methods for simulations depend on the polarizability of the radiation field. In general, vector \mathbf{I} is defined by the Stokes parameters in the polarized radiation field:

$$\mathbf{I} = (I_l, I_r, U, V) \text{ or } (I, Q, U, V). \tag{5}$$

Function $\mathbf{I}(\tau, \Omega)$ is defined as the specific intensity vector at optical depth τ in the direction of Ω , expressed as $\Omega = (\mu, \varphi)$ and $d\Omega = d\mu d\varphi$, where μ is the cosine of the zenith angle θ (i.e., $\mu = \cos \theta$), and φ is the azimuth angle. The RT equation in the plane parallel atmosphere model is described as follows:

$$\mu \frac{d\mathbf{I}(\tau, \Omega)}{d\tau} = \mathbf{I}(\tau, \Omega) - \frac{\omega}{4\pi} \int \tilde{P}(\Omega, \Omega') \cdot \mathbf{I}(\tau, \Omega') d\Omega', \tag{6}$$

where ω and \tilde{P} represent the albedo and phase matrix for single scattering, respectively. Specifically, ω denotes a single scattering albedo (SSA), as shown in Figure 3. Integration was performed over all the solid angles, and the boundary conditions are as follows:

- (1) no radiation falling except in direction Ω_0 at the top of the atmosphere ($\tau = 0$),
- (2) light reflection occurs according to the surface characteristics at the bottom of the atmosphere ($\tau = \tau^*$), wherein τ^* may be regarded as the AOT.

This study uses different RT numerical methods depending on the magnitude of the AOT and the polarization or nonpolarization of the radiation field in order to improve the efficiency and accuracy of aerosol retrieval. The polarization information strongly reflects the aerosol properties, which can be very useful for aerosol retrieval, especially for atmospheres with a moderate AOT. As the SGLI is a multispectral sensor including two polarization channels at PL1 (674 nm) and PL2 (869 nm), efficient and accurate aerosol retrievals can be performed.

First, let us consider the scalar RT method for a high AOT. Biomass burning events generate numerous BBAs. Thus, a significant AOT is expected for the treatment of SBBAs, as shown in the left-side schematic diagram in the bottom section [R] of Figure 3. However, numerical simulations of high-AOT radiation fields are time-consuming and inaccurate. Therefore, such a severely hazy area is usually unprocessed and labeled as “undecided” or “hazy” in the satellite products. In these regions, aerosols and cloud particles seem to mix, allowing a mutual transfer process to occur. As this behavior must be considered, a radiation simulation method is introduced, called the method of successive order of scattering (MSOS). The MSOS used herein is an application of the classical successive scattering method to the calculation of reflected radiation from an optically semi-infinite atmosphere model [34], meaning the MSOS is a successive scattering technique for an optically semi-infinite atmospheric model. A more direct RT approach exists for solving the same problem based on the principle of invariance, in which reflected radiation with the MSOS is called the Chandrasekhar’s H-function [35]. In this scenario, the MSOS effectively calculates the upward intensity of radiation at the top of the atmosphere at $\text{AOT} \approx \infty$, making the MSOS suitable for addressing high AOT cases [23]. Further, as regions classified as SBBAs are optically very thick in the SGLI images, they meet the adaptation requirements of the MSOS, making it a useful RT method for the retrieval of SBBA characteristics. Furthermore, the MSOS does not need to consider the contribution of reflection by the bottom surface, which is helpful as it is difficult for RT simulations to handle the bottom surface reflection according to the actual land use and surface structure in the combined Earth atmosphere–surface system.

In addition, a radiation simulation method using polarized bands, which is one of the features of SGLI, was employed. Herein, the vector type RT simulation referred to as the vector method of adding–doubling (VMAD) [24] was adopted for the atmosphere–surface system, as shown in the right-side schematic diagram in section [R] in the bottom right section of Figure 3. The bottom surface reflection problem previously mentioned cannot be avoided in the vector-type RT problem. Therefore, the polarized reflectance of the bottom surface is considered [36]. The contribution of the bottom surface reflection to the satellite observation decreases with increasing AOT beyond the threshold of approximately $\text{AOT} (550 \text{ nm}) = 1$ in the polarization field [24]. As this represents a rather opaque atmosphere, the bottom surface reflection problem has a small influence on the results. Thus, the polarization information strongly reflects the aerosol properties, and the two polarization channels at PL1(674) and PL2(869) of the SGLI can achieve efficient aerosol retrieval.

4. Results for the Case Study

4.1. Wildfire in Kalimantan, Indonesia

In this section, we describe the properties of BBAs using the methods introduced in Section 3. Asia is not safeguarded from the damage caused by BBAs. Moreover, it is evident that the concentrations of hazardous air pollutants are increasing in Asia owing to increases in anthropogenic aerosol emissions associated with economic growth. Further-

more, yellow dust storms or biomass burning due to agricultural burned fields present serious environmental hazards in East Asia, wherein their aerosol properties are poorly understood. For these reasons, we investigated aerosol remote sensing for severe haze episodes in East Asia [37].

Herein, we selected the Kalimantan wildfire in Indonesia on 15 September 2019 as a case study. In Indonesia, forest fires during the dry season are typical (see case C in Figure 2). However, in 2019, they were abnormally large, causing significant damage to surrounding areas. These Indonesian wildfires caused severe air pollution, which consequently created health hazards that resulted in the deaths of infants and children. In addition, neighboring countries, such as Malaysia and Singapore, were shrouded in thick smog and affected by severe air pollution. Further, the environment was impacted. In particular, Indonesia's rainforests are home to rare plants and animals, including orangutans. Figure 4a shows the color composite image represented by an equal latitude/longitude projection map using unprocessed SGLI/L1 data with a 1 km IFOV. Taking advantage of the SGLI, which has observation channels in the near-UV wavelength, the channels for the three primary colors shifted to shorter wavelengths than usual. Namely, the R, G, and B bands occurred at 443 nm, 412 nm, and 380 nm, respectively. The dark yellow color spreading in the center of the figure denotes the smoke caused by the biomass burning events. In addition, the white beneath the smoke suggests the presence of an optically thick haze. Thus, this scenario is a suitable target for an SBBA analysis, which is confirmed by the distribution of the AAI, as defined in Equation (1), shown in Figure 4b as most of the dark yellow colored area in Figure 4a has AAI values higher than 0.95, which is the threshold value for detecting SBBAs. The open red square in Figure 4a indicates the station Palangkaraya (2.22° S, 113.95° E) of NASA/AERONET.

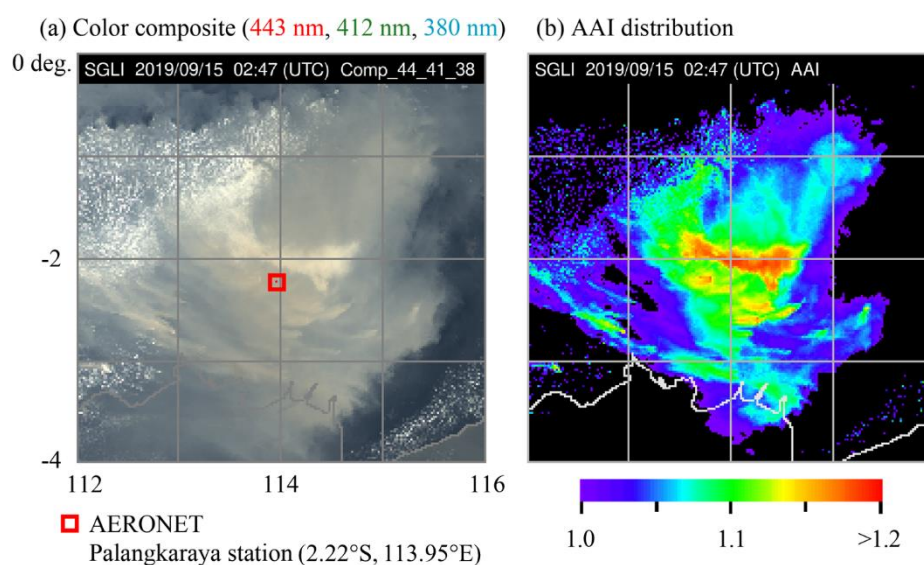


Figure 4. Wildfire events observed from the second-generation global imager (SGLI) over Kalimantan, Indonesia on 15 September 2019. (a) Color composite image. (b) absorbing aerosol index (AAI) distribution.

One characteristic feature of the Kalimantan wildfire that distinguishes it from normal large forest fire is the burning of a tropical peat swamp forest. As shown in Figure 4a, the significant blowdown-like patterns are characteristic of this feature. As the thick peat layer burns, accumulated CO₂ and other greenhouse gases are released into the atmosphere, thereby accelerating global warming and air pollution [38].

4.2. Aerosol Retrieval with Switching RT Simulation

As shown in Figure 5, the sensitivities of the non-PL band (674 nm) and PL band (674 nm) are different. This is likely because the radiance channel considers the observa-

tions of darker targets, such as vegetation and land cover. Thus, the dark violet area in Figure 5a was excluded from the subsequent aerosol retrieval processing. Further, the swaths of both images in Figure 5 are different because of differences in observation angles, wherein the radiance observation telescope observes downward, and the polarization telescope observes at 45° oblique.

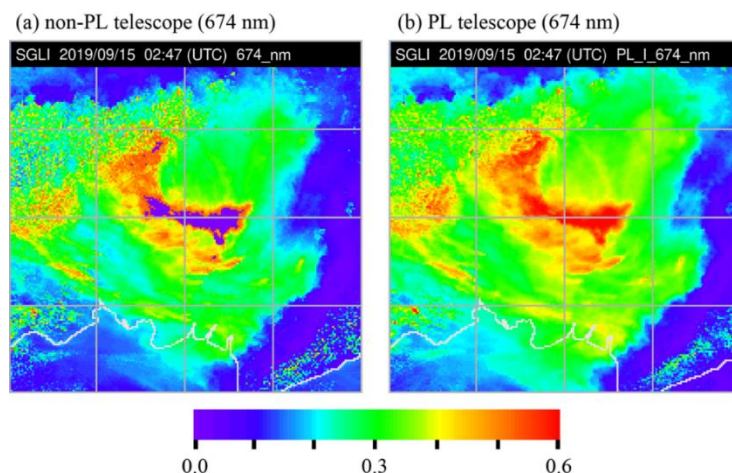


Figure 5. (a) Nonpolarization band (674 nm) and (b) polarization band (PL1; 674 nm) measurements by the second-generation global imager (SGLI) over Kalimantan, Indonesia on 15 September 2020.

These results suggest that it is better to characterize aerosols using polarization data that are suitable for atmospheric observations. However, the SGLI has only two polarization channels. As mentioned in Section 3.2, at least three properties are required to determine the aerosol properties: size (f), composition (g), and optical thickness (AOT). Thus, satellite data from at least three channels are required. Therefore, the radiance channels must be used in addition to the polarization channels. To best utilize the features of the radiance and polarization data, the two should not be used simultaneously. Thus, herein, they are used in stages. Further RT simulation methods, such as the switching system, are also varied in each stage.

4.2.1. RT Simulation with the MSOS for Radiance Data at Short-Wavelength Channels

Heavy smoke, such as SBBAs, is caused by heavy wildfire, as evident from the color composite image shown in Figure 4a. Thus, the MSOS (Section 3.3) was employed for the short-wavelength data at 380 nm, 412 nm, and 443 nm, which are the nonpolarization channels of the SGLI, of which the scalar-type MSOS is applicable. As a result, the values of f , $g1$, and $g2$ described in Section 3.2 can be retrieved. Table 1 lists the resultant wavelength dependence of the aerosol parameters.

Table 1. Wavelength dependence of aerosol parameters used in this work.

Aerosol Properties	Wavelength (nm)								
	380	412	443	530	674	869			
composition: g	←	$g1$	→	←	$g2$	→	←	$g3$	→
size: f	the same value of f								

4.2.2. RT Simulation with VMAD for Polarization Data at PL1 and PL2 Channels

Next, VMAD was applied for the polarization data at bands PL1 and PL2 of the SGLI. The bottom surface reflection is described by the BPDF (bidirectional polarization distribution function) [36]. Using the values of f and $g2$ derived from the MSOS, the values of $g3$ and AOT (869 nm) or AOT (674 nm) can be obtained. Similarly, AOT (443 nm) can be derived using the specific intensity I of the Stokes parameter (I , Q , U , and V) via

the VMAD. Then, AE was calculated for the AOTs (443 nm and 869 nm). The retrieved distributions of the AOT at 674 nm and 869 nm and AE around the NASA/AERONET station of Palangkaraya are shown in Figure 6a–c, respectively.

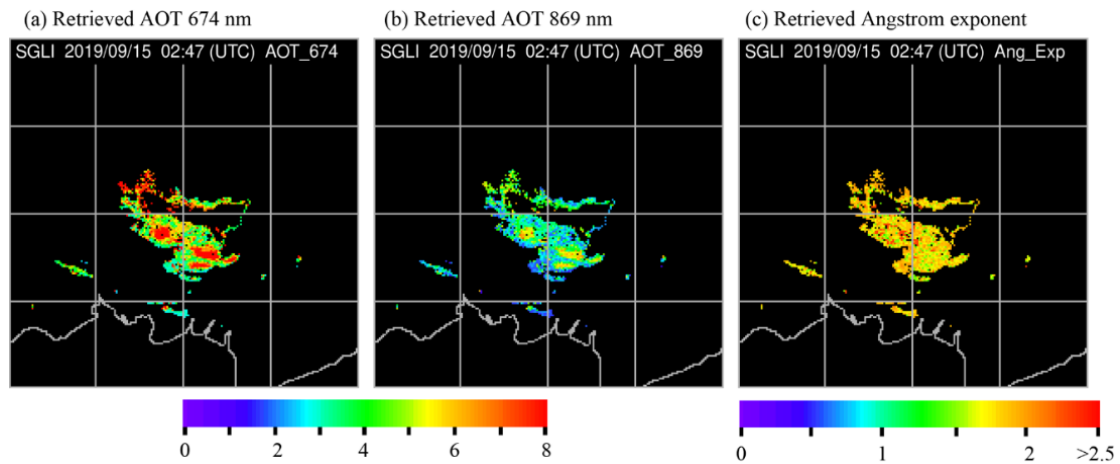


Figure 6. (a,b) Aerosol optical thickness (AOT) and (c) Ångström exponent (AE) retrieved from the second-generation global imager (SGLI) using the vector method of adding–doubling (VMAD) on 15 September 2019.

A comparison of the measurements at the AERONET site, Palangkaraya, is shown in Figure 7. Each error bar represents the standard deviation of the retrieved 3 pixel × 3 pixel near the AERONET station. The obtained AOT values were consistent with the AERONET ground-based observations at both wavelengths. Currently, the maximum value that can be analyzed by AERONET is 7. However, the AOT values for wavelengths shorter than 600 nm are too large to be produced. Thus, the aerosol retrieval algorithm proposed in Section 4.2.1 is validated by the AERONET data. Nevertheless, further comparisons and verifications are necessary. The AE value of approximately 1.7 retrieved from the SGLI is consistent with the ground-based AERONET observation, indicating the presence of small particles.

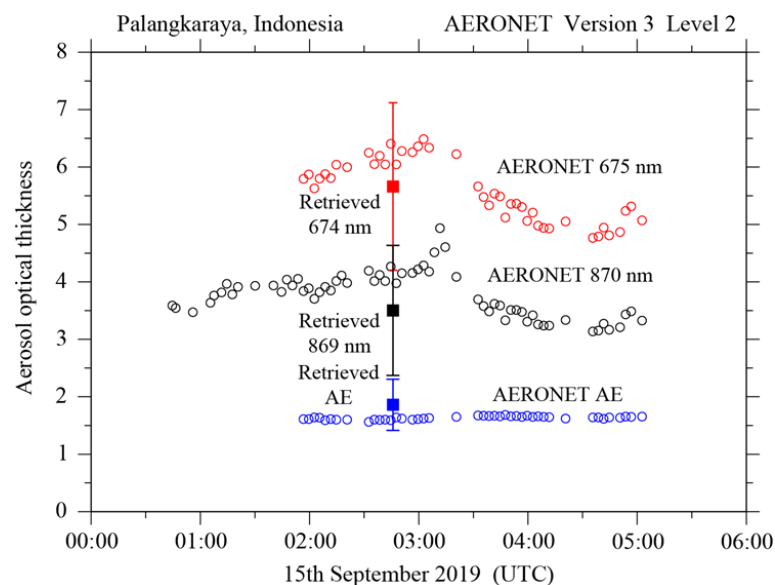


Figure 7. Aerosol optical thickness AOT (674 nm), AOT (869 nm), and Ångström exponent (AE) are depicted as red, black, and blue, respectively. The open circles represent AERONET measurements and the filled squares were retrieved from the second-generation global imager (SGLI) on 15 September 2019.

4.3. Properties of SBBAs

The AOT values at other wavelengths can be derived utilizing the retrieved AE and AOT. Figure 8 presents the AOT distributions of 380 nm, 412 nm, 443 nm, and 530 nm. Note that the color scale in Figure 8 is different from that in Figure 6. The results show that the extreme combustion region had high AOT values, verifying that adopting the MSOS for the 380 nm, 412 nm, and 443 nm channels was suitable for the SBBA analysis.

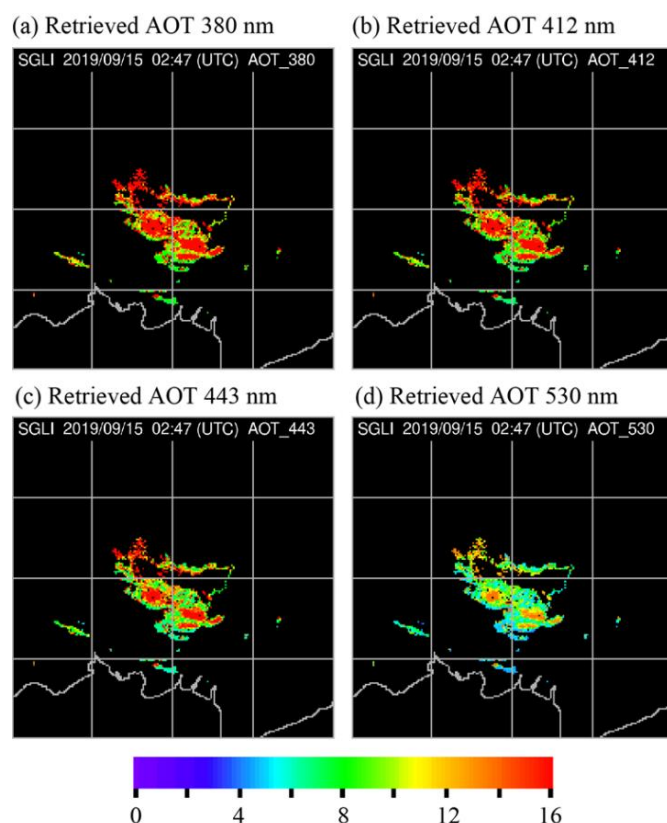


Figure 8. Distribution of aerosol optical thickness (AOT) at (a) 380 nm, (b) 412 nm, (c) 443 nm, and (d) 530 nm.

Finally, the SSA at wavelength λ was calculated from the retrieved f and g values (precisely $g1$, $g2$, and $g3$ in Table 1). The SSA represents the scattering-to-extinction coefficient ratio of the particles in a single light scattering process. While the AE and AOT reflect the results of multiple light scattering between particles in the atmosphere (including reflection processes at the bottom), the SSA represents the optical property of the aerosol itself. The case of $SSA = 1.0$ represents conservative scattering by non-absorbing particles. Figure 9 reveals the retrieved SSA from the SGLI at 380 nm, 412 nm, 443 nm, 530 nm, 674 nm, and 869 nm on 15 September 2019 from around at the Palangkaraya AERONET station. These values were less than 1.0. However, AERONET/SSA measurements were unavailable for 15 September 2019 at Palangkaraya. For reference, the AERONET measurements one day prior (14 September 2019) were depicted by open circles in Figure 10. The filled black squares are the retrieved SSA values from the SGLI on 15 September 2019. Compared with the AERONET, the wavelength dependence of the SSA obtained from the SGLI is slightly sharper and the values are slightly smaller; though, in general, they are in fair agreement. However, even with the AERONET observations, as SSA values fluctuate significantly over time, and a one-day difference can be considered large, the SGLI/SSA values cannot be validated with the ground-based observations. Nevertheless, Figures 6 and 7 reveal that the retrieved AE values were ≥ 1.5 and Figures 9 and 10 reveal that the SSA values were < 1.0 . These results indicate small-sized and light-absorbing particles were present.

The retrieved optical properties represent the characteristics of BBAs well [1,4,39,40]. A closer observation, as shown in Figure 6, Figure 7, Figure 9, and Figure 10, reveals that the particle size and absorption depend on the combustion efficiency, and the distribution suggests that the particle size and absorption of black and brown carbon differ [41–43]. However, more information and a more accurate analysis are required for confirmation.

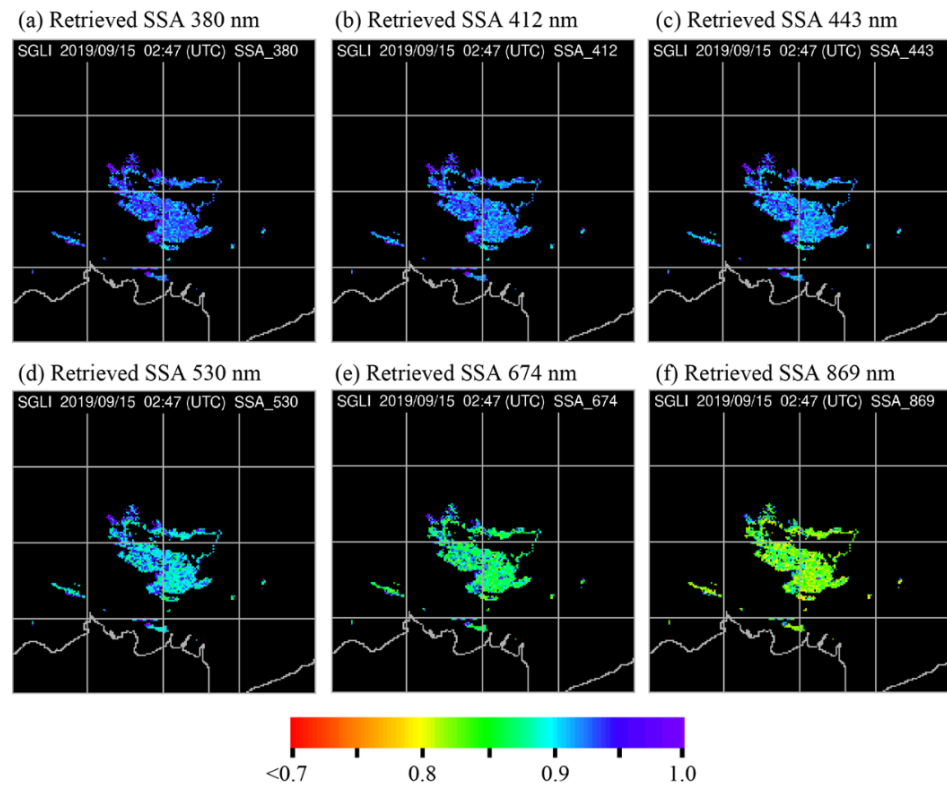


Figure 9. Single scattering albedo (SSA) retrieved from the second-generation global imager (SGLI) data on 15 September 2019 at 380 nm (a), 412 nm (b), 443 nm (c), 530 nm (d), 674 nm (e) and 869 nm (f).

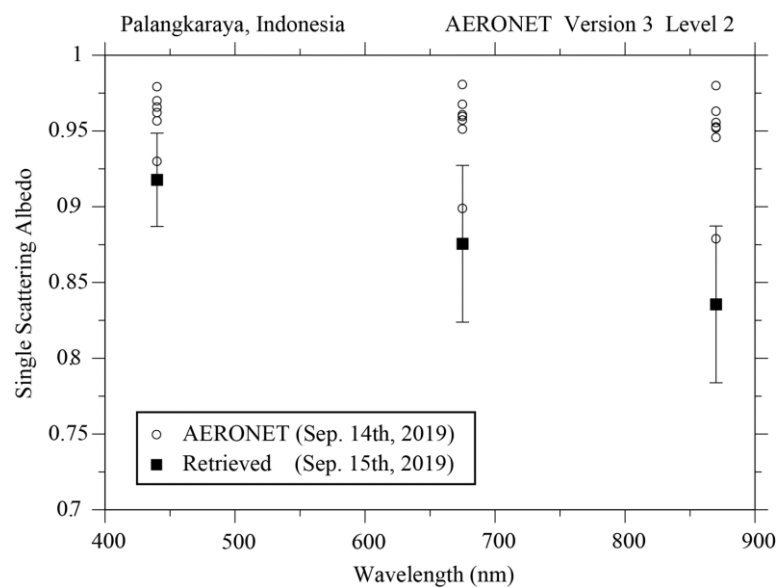


Figure 10. Single scattering albedo (SSA) at 443 nm, 674 nm, and 869 nm. The open circles represent AERONET measurements obtained on 14 September 2019. The filled black squares were retrieved from the second-generation global imager (SGLI) on 15 September 2019.

5. Discussion

The dark violet area in Figure 5a that was excluded during the aerosol retrieval processing may have been clouds or the mixing of clouds and aerosols. The results obtained in Section 4 were compared with the JAXA/SGLI/L2 products. Figure 11 shows the results from JAXA/SGLI/L2 version-1, which focused on the neighboring area of the NASA/AERONET station Palangkaraya (denoted by a small blue square), namely a narrow area near the central area (Figure 4). In the SGLI/L2 version-1, the original 250 m-IFOV data were converted to 1 km² data, and the Sanson projection method was adopted. Figure 11b shows the distribution of the AOT (500 nm) in the color scale and cloud optical thickness (COT (500 nm)) on the gray scale. The cloud phase was classified as only the water cloud. As shown in Figure 11, the dark violet area in Figure 5a was classified as a water cloud. Histograms for the AOT and COT are shown in Figure 11a,c, respectively. Meanwhile, in the L2 version-1, the upper limit of the AOT (500 nm) was set to a value of five, but in reality, it is often saturated at approximately four. For example, the AOT (500 nm) in Figure 11 has a value of less than 3.83. Therefore, the high AOT values shown in Figures 6 and 8 are left undecided in the L2 version-1/AOT (500 nm). These undecided pixels are colored white in Figure 11b. As a result, the AOT (500 nm) at the AERONET station Palangkaraya was also missing in the SGLI/L2, even though the values of the AOT (530 nm) were retrieved (Figure 8). Thus, the retrieved results can be interpreted to compensate for the values in the boundary region between the clouds and aerosols. However, both as a phenomenon and from a measurement standpoint, it is difficult to distinguish clouds and fog at low altitudes from optically thick aerosol layers or haze [39]. Thus, further knowledge of cloud formation and microphysics is necessary to address this problem. More case studies using SGLI data would help to provide a practical solution. Herein, we further considered this problem below using the Japanese geostationary meteorological satellite, Himawari-8/AHI (Advanced Himawari Imager).

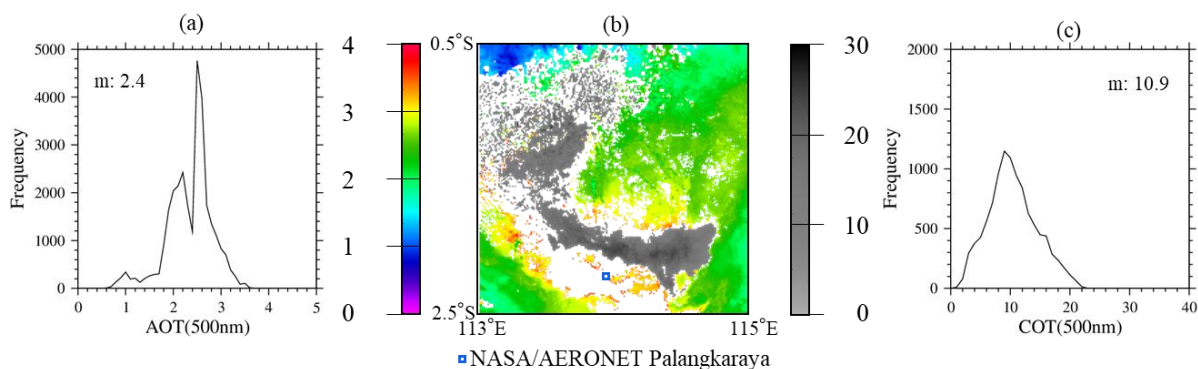


Figure 11. Values of aerosol optical thickness (AOT (500 nm)) (a) and cloud optical thickness (COT (500 nm)) (c) from the JAXA/second-generation global imager (SGLI)/L2 version-1 around the central area of the NASA/AERONET station of Palangkaraya obtained on 15 September 2019. The distribution of AOT (500 nm) and COT (500 nm) is shown in the color scale and gray scale, respectively, in (b).

Figure 12 shows a time-series image from 00:00 to 04:30 on 15 September 2019, as observed by the JMA/Himawari-8/AHI. Figure 12l shows the SGLI image observed at approximately the same time as Figure 12k by Himawari-8/AHI. Strictly speaking in time, Figure 12l,k is inserted between Figure 12f,g. Note that the SGLI channels used to create color composite images in Figure 12l (R, G, and B: 674 nm, 869 nm, and 380 nm, respectively) are different from those in Figure 4a to match the AHI image. It can be seen that the white area in the center of each AHI image appears, disappears, and changes shape in a short period of time. This feature suggests clouds change quickly. While clouds change over time, as they are moving with air masses, the change in shape is not this rapid. Thus, this may be fog rather than clouds. The time variation in the white region can be interpreted as a change in the concentration of atmospheric particles from fog to mist to

haze. In the color composite image from the SGLI in Figure 12l, the smoke from the wildfire is shown in dark yellow due to the assignment of the 380 nm channel to blue. The center of the image is filled in black due to the saturation of channel 674 nm (cf. Figure 5a).

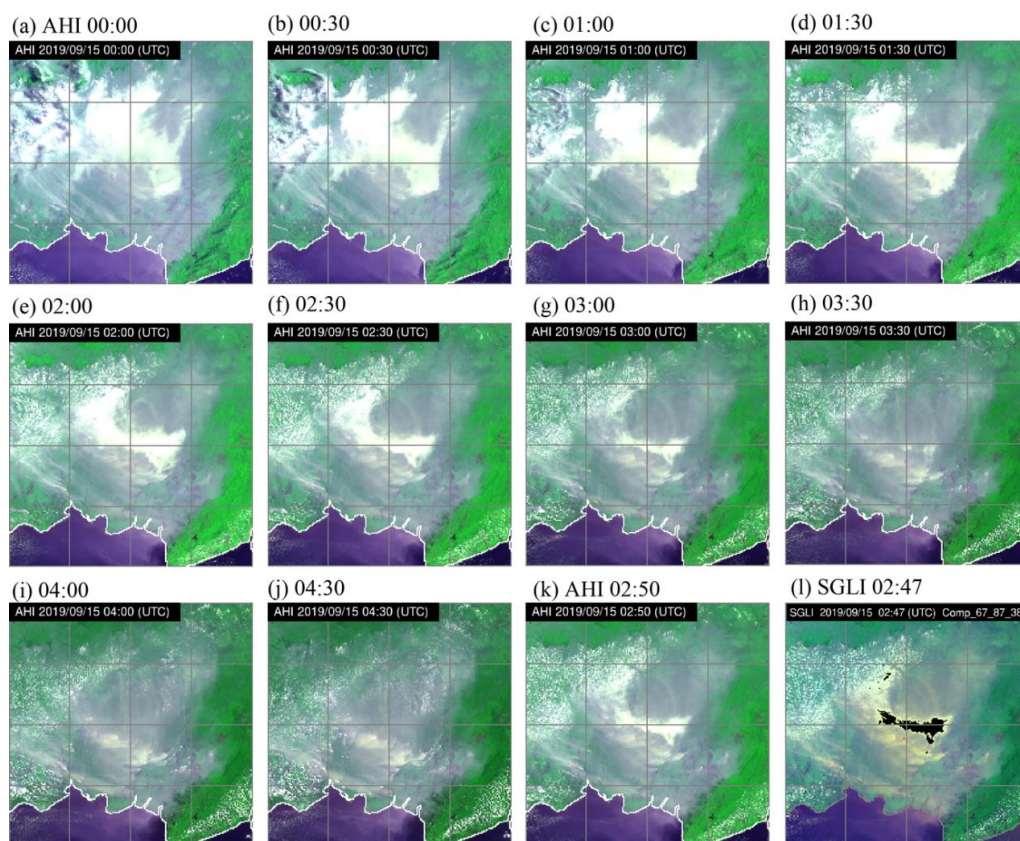


Figure 12. Sequential images at 30-minutes intervals from (a) 00:00 to (j) 04:30 observed by Himawari-8/AHI on 15 September 2019. Note that figure (l) presents the image observed by GCOM-C/SGLI at approximately the same time as that by Himawari-8/AHI in figure (k).

Regardless of whether this area is clouds or haze, the method described herein can be used to analyze atmospheric particles even in the case of optically thick atmospheres that have not yet been determined as SGLI/L2 version-1 products.

6. Conclusions

The characterization process for SBBAs presented herein can be summarized as follows:

1. Detecting SBBAs is based on the expansion of the aerosol type classification method using two types of color ratio indices, the AAI and DDI, which are primarily used for near-UV measurements.
2. The SBBA parameters of f (size distribution) and g (refractive index) are obtained using the radiation MSOS with SGLI radiance data at 380 nm, 412 nm, and 443 nm channels. The aerosol parameters f and g (g_1 and g_2) are obtained.
3. The VMAD is applied to obtain the parameter g_3 in the near-infrared wavelength, and the values of AOT (674 nm) and AOT (869 nm) are determined using the polarization data at bands PL1 (674 nm) and PL2 (869 nm) of the SGLI and the known value of f , and the AOT (443 nm) value is calculated using f and g_2 . Then, the AE value is calculated in terms of AOT (443 nm) and AOT (869 nm).
4. The SSA and AOT at an arbitrary wavelength are calculated utilizing the values retrieved in the previous steps.

Finally, the retrieved results were compared with AERONET ground-based measurements, JAXA/SGLI/L2 version-1 products, and JMA/Himawari-8/AHI observations.

Some of the retrieved aerosol properties were successfully validated, while some remain unconfirmed. Additional case studies would improve our algorithm and make it more conclusive. This work demonstrates the advantages and significance of the multichannel measurement of the GCOM-C/SGLI with polarized and nonpolarized bands used simultaneously for the analysis of severe aerosol events.

Note that satellite remote sensing benefitted heavy air pollution episodes, as demonstrated in Section 4. Although extreme concentrations of aerosols in the atmosphere can prevent aerosol measurements via surface-level photometry, satellites can still be used in such conditions to observe the Earth's atmosphere from space. This is pertinent as it is highly likely that large-scale air pollution will continue to occur. For a better understanding of aerosols, researchers must cross-validate space and ground observations and improve the current algorithms. While large-scale forest fires occur frequently in many parts of the world, as evident in 2019, wildfires are typically short-term regional phenomena. Furthermore, a detailed spatial resolution is required to analyze events [44]. In particular, wildfire-derived particles (BBAs) can enter areas significantly beyond the atmospheric boundary layer. It is necessary to elucidate not only the optical properties of the BBAs presented herein but also their chemical and microphysical properties [40]. In general, a comprehensive analysis of ground/air-based aerosol measurements [45–47], regional numerical simulations [48,49], and satellite observations is desired.

This study suggested what kind of further research should be done. The first step is to implement and validate our algorithm on several severe wildfire cases using GCOM-C/SGLI data. Naturally, dust storms and anthropogenic air pollution must also be taken into account. Then comparison and combination with multi-satellite data is necessary. Next, the similarities and diversity among clouds, fog, mist, haze, and aerosols need to be considered from both theoretical and phenomenological perspectives. As specific tasks, we would like to see addressed the detection of aerosols above clouds and the derivation of aerosol/cloud properties in a combined system of aerosols above clouds.

Author Contributions: Conceptualization, S.M. and M.N.; methodology, S.M.; software, I.S.; validation, I.S.; formal analysis, S.M.; investigation, M.N.; resources, S.M.; data curation, I.S.; writing—original draft preparation, S.M.; writing—review and editing, M.N.; visualization, I.S.; supervision, S.M.; project administration, S.M.; funding acquisition, S.M. and I.S. All authors have read and agreed to the published version of the manuscript.

Funding: This research was funded by the Global Change Observation Mission-Climate project by JAXA (no. JX-PSPC-524344), JSPS KAKENHI Grant Number 19h04242, and the Beyond Europe project (GRASP-cloud) by FFG (Austria).

Acknowledgments: The authors would like to thank Toshiyuki Fujito for assisting in preparing the satellite data, and JAXA, NICT, and CERES/Chiba-U for distributing the observed data with GCOM-C/SGLI and JMA/Himawari-8/AHI, respectively. The authors would also like to thank the PI of the AERONET Palangkaraya station and NASA/AERONET. This study was supported in part by the Global Change Observation Mission-Climate project by JAXA (no. JX-PSPC-524344), JSPS KAKENHI Grant Number 19h04242, and the Beyond Europe project (GRASP-cloud) by FFG (Austria).

Conflicts of Interest: The authors declare no conflict of interest.

References

1. Chen, Y.; Bond, T. Light absorption by organic carbon from wood combustion. *Atmos. Chem. Phys.* **2010**, *10*, 1773–1778. [[CrossRef](#)]
2. Mukai, S.; Yasumoto, M.; Nakata, M. Estimation of Biomass Burning Influence on Air Pollution around Beijing from an Aerosol Retrieval Model. *Sci. World J.* **2014**, *2014*. [[CrossRef](#)]
3. Pyne, S.J. *Between Two Fires: A Fire History of Contemporary America*; University of Arizona Press: Tucson, AZ, USA, 2015.
4. Kalashnikova, O.V.; Garay, M.J.; Bates, K.H.; Kenseth, C.M.; Kong, W.; Cappa, C.D.; Lyapustin, A.; Jonsson, H.H.; Seidel, F.C.; Xu, F.; et al. Photopolarimetric Sensitivity to Black Carbon Content of Wildfire Smoke: Results from the 2016 ImPACT-PM Field Campaign. *J. Geophys. Res.* **2018**, *123*, 5376–5396. [[CrossRef](#)]
5. Dickman, K. The Hidden Toll of Wildfire. *Sci. Am.* **2020**, *322*, 38–45. [[CrossRef](#)]
6. Sokolik, I.; Toon, O. Direct radiative forcing by anthropogenic airborne aerosols. *Nature* **1996**, *381*, 681–683. [[CrossRef](#)]
7. Liao, H.; Seinfeld, J. Effect of clouds on direct aerosol radiative forcing of climate. *J. Geophys. Res.* **1998**, *103*, 3781–3788. [[CrossRef](#)]

8. Quaas, J.; Boucher, O.; Bellouin, N.; Kinne, S. Satellite-based estimate of direct and indirect aerosol climate forcing. *J. Geophys. Res.* **2008**, *113*. [[CrossRef](#)]
9. Jacobson, M. Strong radiative heating due to the mixing state of black carbon in atmospheric aerosols. *Nature* **2001**, *409*, 696–697. [[CrossRef](#)] [[PubMed](#)]
10. IPCC. *Climate Change 2013: The Physical Science Basis. Contribution of Working Group I to the Fifth Assessment Report of the Intergovernmental Panel on Climate Change*; Cambridge University Press: Cambridge, UK, 2013; p. 1585.
11. Stohl, A.; Berg, T.; Burkhardt, J.F.; Fjaraa, A.M.; Forster, C.; Herber, A.; Hov, O.; Lunder, C.; McMillan, W.W.; Oltmans, S.; et al. Arctic Smoke—Record high air pollution levels in the European Arctic due to agricultural fires in Eastern Europe. *Atmos. Chem. Phys.* **2007**, *7*, 511–534. [[CrossRef](#)]
12. Ten Hoeve, J.E.; Remer, L.A.; Jacobson, M.Z. Microphysical and radiative effects of aerosols on warm clouds during the Amazon biomass burning season as observed by MODIS impacts of water vapor and land cover. *Atmos. Chem. Phys.* **2011**, *11*, 3021–3036. [[CrossRef](#)]
13. Kinne, S.; Lohmann, U.; Feichter, J.; Schulz, M.; Timmreck, C.; Ghan, S.; Easter, R.; Chin, M.; Ginoux, P.; Takemura, T.; et al. Monthly averages of aerosol properties: A global comparison among models, satellite data and AERONET ground data. *J. Geophys. Res.* **2003**, *108*, 4634. [[CrossRef](#)]
14. Sokolik, I.; Winker, D.; Bergametti, G.; Gillette, D.; Carmichael, G.; Kaufmann, Y.; Gomes, L.; Shuetz, L.; Penner, J. Introduction to special section: Outstanding problems in quantifying the radiative impacts of mineral dust. *J. Geophys. Res.* **2001**, *106*, 18015–18027. [[CrossRef](#)]
15. Levy, R.; Remer, L.; Tanre, D.; Kaufman, Y.; Ichoku, C.; Holben, B.; Livingston, J.; Russell, P.; Maring, H. Evaluation of the Moderate-Resolution Imaging Spectroradiometer (MODIS) retrievals of dust aerosol over the ocean during PRIDE. *J. Geophys. Res.* **2003**, *108*. [[CrossRef](#)]
16. Zhang, J.; Christopher, S. Longwave radiative forcing of Saharan dust aerosols estimated from MODIS, MISR, and CERES observations on Terra. *Geophys. Res. Lett.* **2003**, *30*, 2188. [[CrossRef](#)]
17. Li, F.; Vogelmann, A.; Ramanathan, V. Saharan Dust Aerosol Radiative Forcing Measured from Space. *J. Clim.* **2004**, *17*, 2558–2571. [[CrossRef](#)]
18. Littmann, T. Dust storm frequency in Asia: Climatic control and variability. *Int. J. Climatol.* **1991**, *11*, 393–412. [[CrossRef](#)]
19. Lee, K.; Kim, Y. Satellite remote sensing of Asian aerosols: A case study of clean, polluted, and dust storms. *Atmos. Meas. Tech.* **2010**, *3*, 1771–1784. [[CrossRef](#)]
20. Eck, T.; Holben, B.; Reid, J.; Dubovik, O.; Smirnov, A.; O'Neill, N.; Slutsker, I.; Kinne, S. Wavelength dependence of the optical depth of biomass burning, urban and desert dust aerosols. *J. Geophys. Res.* **1999**, *104*, 31333–31350. [[CrossRef](#)]
21. Mukai, S.; Sano, I.; Nakata, M. Algorithms for the classification and characterization of aerosols: Utility verification of near-UV satellite observations. *J. Appl. Remote Sens.* **2019**, *13*, 014527. [[CrossRef](#)]
22. Mukai, S.; Sano, I.; Nakata, M. Effective characterization of aerosols in severe events using multi-channel measurements including polarization with GCOM-C/SGLI. In Proceedings of the SPIE 11531, Remote Sensing of Clouds and Atmosphere XXV, Edinburgh, UK, 21–25 September 2020; p. 115310Q. [[CrossRef](#)]
23. Mukai, S.; Yokomae, T.; Nakata, M.; Kohkanovsky, A. Multiple scattering in a dense aerosol atmosphere. *Atmos. Meas. Tech. Discuss.* **2012**, *5*, 881–907.
24. Mukai, S.; Sano, I.; Takashima, T. Investigation of atmospheric aerosols based on polarization measurements and scattering simulations. *Opt. Rev.* **1996**, *3*, 487–491. [[CrossRef](#)]
25. Mukai, S.; Nakata, M.; Fujito, T.; Sano, I. Efficient Detection of Aerosols Above Clouds Utilizing GCOM-C/SGL Data. *Int. J. Environ. Monit. Anal.* **2020**, *8*, 170–180. [[CrossRef](#)]
26. O'Neill, N.; Dubovik, O.; Eck, T. Modified Angstrom exponent for the characterization of submicrometer aerosols. *Appl. Opt.* **2001**, *40*, 2368–2375. [[CrossRef](#)]
27. Omar, A.; Won, J.; Winker, D.; Yoon, S.; Dubovik, O.; McCormick, P. Development of global aerosol models using cluster analysis of aerosol robotic network (AERONET) measurements. *J. Geophys. Res.* **2005**, *110*, 10–14. [[CrossRef](#)]
28. Torres, O.; Bhartia, P.; Herman, J.; Ahmad, Z.; Gleason, J. Derivation of aerosol properties from satellite measurements of backscattered ultraviolet radiation: Theoretical basis. *J. Geophys. Res.* **1998**, *103*, 17099–17110. [[CrossRef](#)]
29. de Graaf, M.; Stammes, P.; Torres, O.; Koelemeijer, R.B.A. Absorbing Aerosol Index: Sensitivity analysis, application to GOME and comparison with TOMS. *J. Geophys. Res.* **2005**, *102*. [[CrossRef](#)]
30. Ciren, P.; Kondragunta, S. Dust aerosol index (DAI) algorithm for MODIS. *J. Geophys. Res.* **2014**, *119*, 4770–4792. [[CrossRef](#)]
31. Bohren, C.; Wickramasinghe, N. On the Computation of Optical Properties of Heterogeneous Grains. *Astrophys. Space Sci.* **1977**, *50*, 461–472. [[CrossRef](#)]
32. Bond, T.; Bergstrom, R. Light Absorption by Carbonaceous Particles: An Investigative Review. *Aerosol Sci. Technol.* **2007**, *40*, 27–67. [[CrossRef](#)]
33. Sayer, A.; Hsu, N.; Eck, T.; Smirnov, A.; Holben, B. AERONET-based models of smoke-dominated aerosol near source regions and transported over ocean, and implications for satellite retrievals of aerosol optical depth. *Atmos. Chem. Phys.* **2014**, *14*, 11493–11523. [[CrossRef](#)]
34. Uesugi, A.; Irvine, W. Multiple scattering in a plane-parallel atmosphere I. Successive scattering in a semi-infinite medium. *Astrophys. J.* **1970**, *159*, 127–135. [[CrossRef](#)]

35. Chandrasekhar, S. *Radiative Transfer*; Dover Publications, Inc.: New York, NY, USA, 1960; Chapter V.
36. Nadal, F.; Bréon, F.M. Parameterization of surface polarized reflectance derived from POLDER space-borne measurements. *IEEE Trans. Geosci. Remote Sens.* **1999**, *37*, 1709–1718. [[CrossRef](#)]
37. Nakata, M.; Sano, I.; Mukai, S.; Holben, B. Spatiotemporal variations in atmospheric aerosols in East Asia: Identifying local pollutants and transported Asian aerosols in Osaka, Japan using DRAGON. *Atmos. Chem. Phys. Discuss.* **2016**. [[CrossRef](#)]
38. Yulianti, N.; Hayasaka, H. Recent active fire under El Niño conditions in Kalimantan, Indonesia. *Am. J. Plants Sci.* **2013**, *4*, 685–696. [[CrossRef](#)]
39. Eck, T.; Holben, B.; Reid, J.; O’Niel, N.; Schafer, J.; Dubovik, O.; Smirnov, A.; Yamasoe, M.; Artaxo, P. High aerosol optical depth biomass burning events: A comparison of optical properties for different source regions. *Geophys. Res. Lett.* **2003**, *30*. [[CrossRef](#)]
40. Chen, W.; Kahn, R.; Nelson, D.; Yau, K.; Seinfeld, J. Sensitivity of multineedle imaging to the optical and microphysical properties of biomass burning aerosols. *J. Geophys. Res.* **2008**, *113*, D10203. [[CrossRef](#)]
41. Chakrabarty, R.; Moosmuller, H.; Chen, L.; Lewis, K.; Arnott, W.; Mazzoleni, C.; Dubey, M.; Wold, C.; Hao, W.; Kreidenweiss, S. Brown carbon in tar balls from moldering biomass combustion. *Atmos. Chem. Phys.* **2010**, *10*, 6363–6370. [[CrossRef](#)]
42. Shi, S.; Cheng, T.; Gu, X.; Guo, H.; Wu, Y.; Wang, Y. Biomass burning aerosol characteristics for different vegetation types in different aging periods. *Environ. Int.* **2019**, *126*, 504–511. [[CrossRef](#)]
43. Noyes, K.; Kahn, R.; Sedlacek, A.; Kleinman, L.; Limbacher, J.; Li, Z. Wildfire Smoke Particle Properties and Extrusion, from Space-Based Multi-Angle Imaging. *Remote Sens.* **2020**, *12*, 769. [[CrossRef](#)]
44. Vay, S.; Woo, J.; Anderson, B.; Thornhill, K.; Blake, D.; Westberg, D.; Kiley, C.; Avery, M.; Sachse, G.; Streets, D.; et al. Influence of regional-scale anthropogenic emissions on CO₂ distributions over the western North Pacific. *J. Geophys. Res.* **2003**, *108*, 8801. [[CrossRef](#)]
45. Sano, I.; Mukai, S.; Nakata, M.; Holben, B. Regional and local variations in atmospheric aerosols using ground-based sun photometry during Distributed Regional Aerosol Gridded Observation Networks (DRAGON) in 2012. *Atmos. Chem. Phys.* **2016**, *16*, 14795–14803. [[CrossRef](#)]
46. Holben, B.; Kim, J.; Sano, I.; Mukai, S.; Eck, T.; Giles, D.; Schafer, J.; Sinyuk, A.; Slutsker, I.; Smirnov, A.; et al. An overview of mesoscale aerosol processes, comparison, and validation studies from DRAGON networks. *Atmos. Chem. Phys.* **2018**, *18*, 655–671. [[CrossRef](#)]
47. Noyes, J.; Kahn, R.; Limbacher, J.; Li, Z.; Fenn, M.; Giles, D.; Hair, J.; Katich, J.; Moore, R.; Robinson, C.; et al. Wildfire Smoke Particle Properties and Evolution, From Space-Based Multi-Angle Imaging II: The Williams Flats Fire during the FIREX-AQ campaign. *Remote Sens.* **2020**, *12*, 3823. [[CrossRef](#)]
48. Nishizawa, S.; Yashiro, H.; Sato, Y.; Miyamoto, Y.; Tomita, H. Influence of grid aspect ratio on planetary boundary layer turbulence in large-eddy simulations. *Geosci. Model Dev.* **2015**, *8*, 3393–3419. [[CrossRef](#)]
49. Kajino, M.; Deushi, M.; Sekiyama, T.; Oshima, N.; Yumimoto, K.; Tanaka, T.Y.; Ching, J.; Hashimoto, A.; Yamamoto, T.; Ikegami, M.; et al. NHM-Chem, Japan meteorological agency’s regional meteorology—Chemistry model: Model evaluations toward the consistent predictions of the chemical, physical, and optical properties of aerosols. *J. Meteorol. Soc. Jpn.* **2019**, *97*, 337–374. [[CrossRef](#)]